ADVANCED FUNCTIONAL MATERIALS
www.afm-journal.de

Silver Clusters of Five Atoms as Highly Selective Antitumoral Agents Through Irreversible Oxidation of Thiols

Vanesa Porto, David Buceta, Blanca Domínguez, Carmen Carneiro, Erea Borrajo, María Fraile, Nerea Davila-Ferreira, Iria R. Arias, José M. Blanco, Maria C. Blanco, Juan M. Devida, Lisandro J. Giovanetti, Félix G. Requejo, Juan C. Hernández-Garrido, José J. Calvino, Miguel López-Haro, Giampaolo Barone, Andrew M. James, Tomás García-Caballero, Diego M. González-Castaño, Martin Treder, Wolfgang Huber, Anxo Vidal, Michael P. Murphy, M. Arturo López-Quintela, and Fernando Domínguez**

Low atomicity clusters present properties dependent on the size, due to the quantum confinement, with well-defined electronic structures and high stability. Here it is shown that Ag_5 clusters catalyze the complete oxidation of sulfur to S^{+6}. Ag_5 catalytic activity increases with different oxidant species in the order $O_2 \ll H_2O_2 < OH\bullet$. Selective oxidation of thiols on the cysteine residues of glutathione and thioredoxin is the primary mechanism human cells have to maintain redox homeostasis. Contingent upon oxidant concentration, Ag_5 catalyzes the irreversible oxidation of glutathione and thioredoxin, triggering apoptosis. Modification of the intracellular environment to a more oxidized state to mimic conditions within cancer cells through the expression of an activated oncogene ($HRAS^{G12V}$) or through ARID1A mutation, sensitizes cells to Ag_5 mediated apoptosis. While cancers evolve to evade treatments designed to target pathways or genetic mutations that drive them, they cannot evade a treatment that takes advantage of aberrant redox homeostasis, which is essential for tumor progression and metastasis. Ag_5 has antitumor activity in mice with orthotopic lung tumors reducing primary tumor size, and the burden of affected lymphatic nodes. The findings suggest the unique intracellular redox chemistry of Ag_5 may lead to new redox-based approaches to cancer therapy.

1. Introduction

The mitochondrial electron transport chain is indispensable for cell proliferation,[1–4] generating as by-product reactive oxygen species (ROS).[5,6] H_2O_2 sensors measure H_2O_2 concentration by a redox-based mechanism and set H_2O_2 -specific scavengers' expression, maintaining the H_2O_2 concentration below a toxic threshold.[7] Thiol redox status within mitochondria, is determined by the mitochondrial glutathione (GSH) and thioredoxin (Trx) systems, critical for cell viability and function.[8] Simultaneous and irreversible inhibition of these pathways could constitute an effective antitumor treatment.[9] Of interest, Au clusters with 5–10 atoms can catalyze the aerobic oxidation of thiophenol to disulfide (S^{-2} to S^{-1}) at room temperature and 5 bar O_2 with similar catalytic activity to the sulfhydryl oxidase.[10] Metal clusters of just a few atoms can display unique properties that are not observed

V. Porto, C. Carneiro, E. Borrajo, M. Fraile, N. Davila-Ferreira, A. Vidal, F. Domínguez
Department of Physiology and Centro de Investigaciones en Medicina Molecular y Enfermedades Crónicas (CIMUS)
IDIS
Universidade de Santiago de Compostela
Santiago de Compostela 15782, Spain
E-mail: fernando.dominguez@usc.es

The ORCID identification number(s) for the author(s) of this article can be found under https://doi.org/10.1002/adfm.202113028.

DOI: 10.1002/adfm.202113028

D. Buceta, B. Domínguez, I. R. Arias, J. M. Blanco, M. C. Blanco, M. A. López-Quintela
Departments of Physical Chemistry and Applied Physics
Nanomag Laboratory
IIT
Universidade de Santiago de Compostela
Santiago de Compostela 15782, Spain
E-mail: malopez.quintela@usc.es

J. M. Devida, L. J. Giovanetti, F. G. Requejo
Instituto de Investigaciones Fisicoquímicas Teóricas y Aplicadas (INIFTA)
(FCE, UNLP and CONICET)
La Plata 1900, Argentina

J. C. Hernández-Garrido, J. J. Calvino, M. López-Haro
Department of Material Science and Metallurgic Engineering and Inorganic Chemistry
Faculty of Science
University of Cadiz
Puerto Real (Cádiz), Cádiz 11510, Spain

in larger nanoparticles.[11–14] Reducing cluster size from the bulk material to the subnanometric cluster scale alters the particle properties which are greatly affected by strong quantum confinement. Those cluster properties depend strongly on the number of atoms. Here we show that contrary to smaller Ag_3 clusters, which do not bind to thiols but intercalate into DNA,[14,15] Ag_5, with only two more atoms, binds to thiols and display exceptional catalytic activities for their complete oxidation. Contingent upon oxidant concentration, Ag_5 catalyzes the oxidation of cysteine (Cys), GSH, and Trx successively to disulfide (S^{-1}), sulfinic (S^{+2}), sulfonic (S^{+4}), and finally irreversibly detaches the sulfur atom from the rest of the molecule and oxidizing it to sulfate (S^{+6}). Having shown that Ag_5 affects thiol-based antioxidants, we hypothesized that this could be effectively employed for novel pharmacological applications where redox state is important, such as in cancer.[16,17] We present here that Ag_5, depending on the intracellular redox state, catalyzes the oxidation of redox-active Cys residues, leading to the activation of programmed cell death. We further describe driven mutations frequently found in human cancers that render cells sensitive to Ag_5.

2. Results and Discussion

2.1. Ag_5 Catalyze the Oxidation of Cysteine

Ag_5 was synthesized by a modification of a previously developed electrochemical method for the synthesis of Ag_3.[14,15] As we describe in the Experimental Section, we increased the voltage with respect to the preparation of Ag_3 clusters. This allows to focus the kinetics to produce Ag_5 clusters mainly. When the voltage is further increased (see the Experimental Section) larger clusters are obtained. Interestingly such larger clusters do not display the catalytic activities here described for Ag_5 but act specifically in the lysosomes and do not cause cell mortality as it will be reported elsewhere.

Ag clusters were fully characterized by high-angle dark-field scanning transmission electron microscopy (HAADF-STEM) (see Characterization of Ag_5 and Figures S1 and S2, Supporting Information), UV–Vis, and fluorescence spectroscopy (see Characterization of Ag_5 and Figures S3 and S4, Supporting Information), electrospray ionization time-of-flight (ESI-TOF) mass spectrometry (see Characterization of Ag_5 and Figures S5 and S6, Supporting Information), X-ray absorption near edge structure (XANES) (see Characterization of Ag_5 and Figure S7, Supporting Information). All characterization techniques indicate that samples contain mainly Ag_5, with a small percentage (≤10%) of noncatalytic smaller Ag_3 and Ag_2 clusters, because they do not bind S groups, as we reported before.[14,15]

Using X-ray absorption near-edge structure at the sulfur K edge (S-K XANES), we assessed the effect of Ag_5 on the oxidation of the sulfur groups of free Cys, GSH, and recombinant *Escherichia coli* Trx. The R-SH groups of these three species were oxidized to S^{+6} (sulfate) in the presence of Ag_5 at very low concentration (1000 times less than R-SH, $[R\text{-}SH]/[Ag_5] \approx 1000$) after 10 min of reaction (**Figure 1**a). The gradual increase in the S^{+6} peak relative to the S^{-2} peak with increasing Ag_5 concentration (Figure 1b) is indicative of the SH oxidation reaction dependence on the Ag_5 concentration (see XANES study of Ag_5 catalysis, Table S1 and Figures S8–S10, Supporting Information). Thus, Ag_5 catalyzes R-SH overoxidation until a biological irreversible state (S^{+5} or S^{+6}).[18] When the concentration of Ag_5 is reduced ($[R\text{-}SH]/[Ag_5] < \approx 10\,000$) Ag_5 still catalyzes the oxidation of sulfur groups but only to form disulfides (S^{-1}), at the same time of reaction. As far as we know, there is no catalyst that can totally oxidize sulfur groups with atmospheric oxygen, indicating the high catalytic activity of Ag_5 clusters. Moreover, the catalytic activity of Ag_5 for the partial sulfur oxidation to disulfide is ($TOR \approx 3 \times 10^3\ s^{-1}$) ≈ 2 orders of magnitude larger than the one reported previously for Au clusters,[10] as we will report elsewhere. Using intermediate concentrations of clusters, in the range ($[R\text{-}SH]/[Ag_5] \approx 1000$–$10\,000$), at the same reaction time, we obtain a population of different oxidation species, namely, S^{-1}, S^{+2}, S^{+4}, and S^{+6} (see XANES study of Ag_5 catalysis and Figure S11, Supporting Information).

We used density-functional theory (DFT) to determine the possible mechanism by which S-containing compounds are oxidized catalytically by Ag_5 (Figure 1c,d). First, we found that Ag_5 can adsorb oxygen molecules, activating some of them to superoxide-like species (see Theoretical Calculations, Table S2 and Figures S12–S19, Supporting Information). Using such activated oxygens, Ag_5 forms, in a fast step, a disulfide (Figure 1c). Subsequently, as we can see in Figure 1d, the activated oxygens are able to break the S–S bond with the formation of R-$(SO)_2$-Ag_5 sulfinic species (I3, S^{+2}) attached to the cluster. Such sulfinic species can be further catalytically overoxidized to sulfite R-(SO_3)-Ag_5 (I5, S^{+4}) and finally, detaching the S from the rest of the organic molecule, (SO_3)-Ag_5 (I6), to sulfate (SO_4)-Ag_5 (P, S^{+6}) species.

2.2. Other Oxidants Involved in Ag_5 Catalysis

Oxidants other than O_2 could also be involved in the catalytic activity of Ag_5 under biological conditions and understanding their impact could help elucidate whether Ag_5 has clinical applications.[19] Therefore, we investigated the catalytic activity by XANES of Ag_5 against recombinant *E. coli* Trx in the presence of H_2O_2 or the hydroxyl radical (OH•). Due to the higher oxidation activity of these species,

G. Barone
Department of Biological, Chemical and Pharmaceutical Sciences and Technologies
University of Palermo
Palermo 90128, Italy

A. M. James, M. P. Murphy
MRC Mitochondrial Biology Unit
University of Cambridge
Cambridge CB2 0XY, UK

T. García-Caballero
Department of Morphological Sciences
School of Medicine-University Clinical Hospital
Universidade de Santiago de Compostela
Santiago de Compostela 15782, Spain

D. M. González-Castaño
Radiation Physics Laboratory
RIAIDT
Universidade de Santiago de Compostela
Santiago de Compostela 15782, Spain

M. Treder
Arjuna Therapeutics
Milladoiro 15895, Spain

W. Huber
European Molecular Biology Laboratory (EMBL)
69115 Heidelberg, Germany

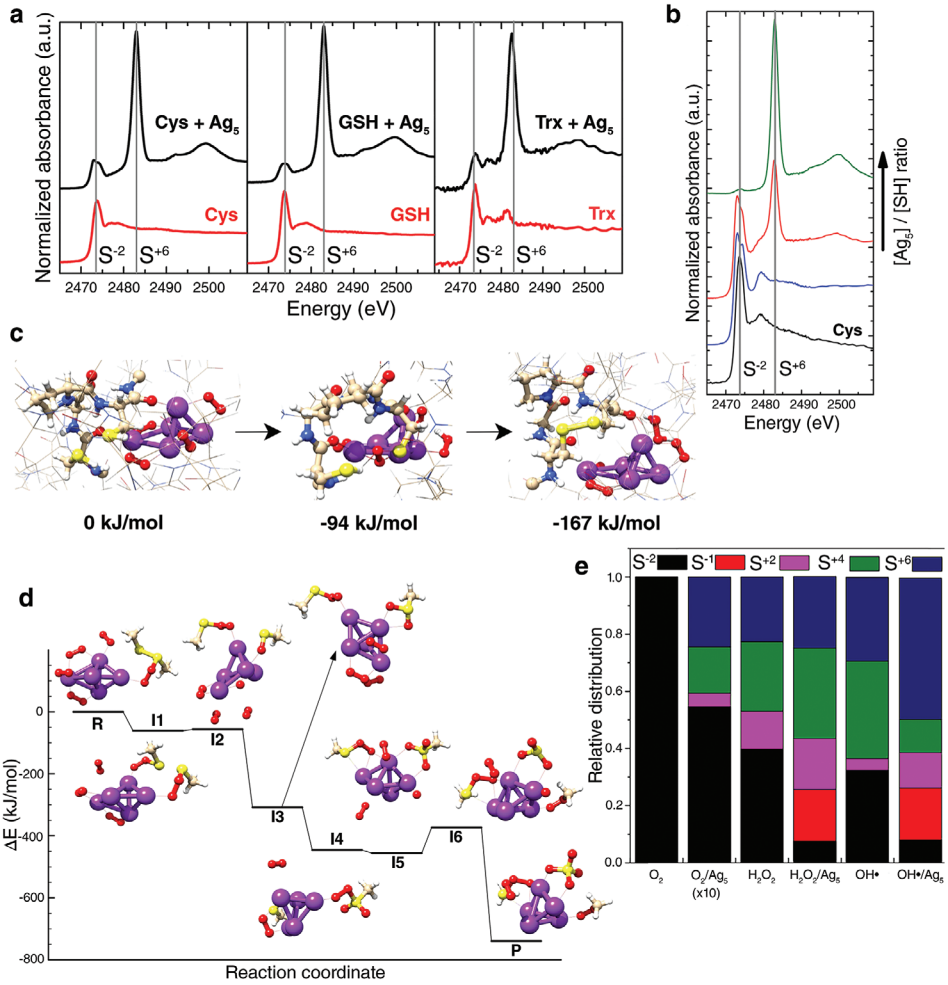

Figure 1. Ag_5 catalyze R-SH oxidation. a) Normalized S-K XANES spectra of cysteine (Cys), glutathione (GSH) and thioredoxin (Trx) before and after addition of Ag_5. Vertical lines indicate the corresponding energy for different S-oxidation states. b) Normalized S-K XANES spectra of Cys after addition of increasing concentrations of Ag_5. Vertical lines indicate the energy position associated to the different S-oxidation states. c) Proposed DFT mechanism for the formation of a disulfide on oxygenated Ag_5. d) Proposed DFT mechanism for S–S bond breaking and subsequent formation of sulfinic, sulfite, and sulfate on Ag_5. e) Population of S-oxidized species for thioredoxin (Trx) with different oxidating species, obtained from S K-XANES for $[Ag_5]/[Trx] = 1:5000$, after 10 min of reaction.

we carried out the experiments, at 10 min of reaction time, with concentrations of oxidants 10 times less than oxygen and a ratio $[R\text{-}SH]/[Ag_5] = 5000$. For comparison purposes (Figure 1e), at the same conditions, when exogeneous oxygen is present with clusters we observe the formation of ≈4% of the S in an oxidation state > = –1 (1.6% S^{+4} and 2.4% S^{+6}, i.e., 16% and 24% without concentration correction, displayed in Figure 1e for a better visualization) versus 0% without clusters. We show also that H_2O_2 without clusters oxidizes 60% (25% S^{+4} and 22% S^{+6}) of recombinant *E. coli* Trx, while with clusters this proportion increases to 92% (31% S^{+4} and 26% S^{+6}). When using OH• the oxidized proportion is 88% (34% S^{+4} and 29% S^{+6}) while with clusters is 92% (12% S^{+4} and 50% S^{+6}). Therefore, we can conclude that the catalytic activity of Ag_5 increases with different oxidant species in the order $O_2 \ll H_2O_2 <$OH•.

2.3. Cellular Ag_5 Uptake

To assess the ability of Ag_5 to enter cancer cells, we incubated human acute lymphoblastic leukemia MOLT-4 cells with Ag_5 at 37 °C. After 5 min incubation at 37 °C, 14% ± 1.72 SEM of the total silver offered to the cells was found inside the cell (see Figure S20a,b, Supporting Information). To elucidate the mechanism of Ag_5 transport across the plasma membrane, we compared the uptake of Ag_5 in MOLT-4 cells at 4 and 37 °C. There was no difference with temperature indicating Ag_5 transport is a passive rather than an active process (see Figure S20c, Supporting Information). Moreover, modification of the mitochondrial membrane potential did not alter the amount of silver in isolated mitochondria after Ag_5 treatment (see Figure S20d, Supporting Information). Together, these data suggest that Ag_5 can enter cells and mitochondria by passive diffusion as an uncharged species.

2.4. Ag_5 Increases Intracellular Thiol Oxidation

As Ag_5 oxidizes thiols in vitro and can diffuse into cells we sought to demonstrate that Ag_5 could oxidize intracellular thiols. We observed a significant reduction (≈20%) in the

intracellular GSH/GSSG ratio in whole-cell lysates of A549 cells treated with Ag_5 for 1 h (see Figure S21, Supporting Information). Glutathione reductase (GR) maintains the ratio of GSH/GSSG present in the cell by catalyzing the reduction of GSSG to GSH.[20] Western blotting of whole-cell lysates of A549 cells revealed a rapid and substantial increase in the oxidized GR form following stimulation with Ag_5 (**Figure 2**a). This suggests that Ag_5 may accelerate thiol oxidation by targeting sensitive thiols on redox enzymes, thereby tipping the balance toward the oxidative state. To elucidate time-dependent changes of thiol oxidation by Ag_5 we used a redox sensitive glutaredoxin-1 (Grx1)-roGFP biosensor designed to specifically measure the GSH redox potential.[21] The addition of Ag_5 to A549 cells led to a prompt oxidative response with the maximum signal observed after 7 min (Figure 2b) revealing Ag_5 rapidly mediated thiol oxidation catalysis.

2.5. Ag_5 Increases the Oxidation of Thioredoxin-Dependent Peroxiredoxin 3 (PRDX3) in A549 Lung Carcinoma Cells Mitochondria

As shown by XANES experiments, Ag_5 increases oxidation of thiol groups of *E. coli* recombinant Trx. Furthermore, QM/MM calculations confirmed the binding of Ag_5 in the Cys-X-X-Cys motif of the Trx (see Theoretical Calculations, Supporting Information). Additionally, in an in vitro assay, Ag_5 strongly inhibited the Trx/thioredoxin reductase (TrxR) system (Figure 2c) (see Ag_5 catalyze Trx and TrxR and Figure S22, Supporting Information). Grx1 also possesses the Trx motif Cys-X-X-Cys,[22] so the observed activation in the Grx1-roGFP biosensor might also be due to the direct effect of Ag_5 mediated oxidation of the Cys residues in Grx1. Therefore, we explored whether Ag_5 also affected the Trx antioxidant system in cells. Trx oxidation depends on H_2O_2 and PRDX3, an enzyme located exclusively in the mitochondrial matrix that reacts rapidly with H_2O_2 and dimerizes via a disulfide.[23,24] Mitochondria isolated from Wistar rats' heart and liver were incubated with Ag_5 at different doses for 5 min at 37 °C. As shown in Figure 2d, PRDX3 oxidation was dependent on the Ag_5 concentration ($(40–240) \times 10^{-9}$ M). In contrast, Ag^+ at the largest concentration of Ag_5 used did not affect the PRDX3 redox state. This finding confirms the membrane permeability of Ag_5, as it must have crossed the inner mitochondrial membrane to oxidize PRDX3. Furthermore, 15 min after intact cells were exposed to Ag_5, PRDX3 was oxidized (Figure 2e), confirming that Ag_5 rapidly diffuses into the cell, enter the mitochondria, and increases the oxidation of PRDX3.

2.6. Ag_5 is Cytotoxic for Human Cancer Cells

A chemical disrupting redox homeostasis would be expected to induce cell death. Treatment of A549 human lung adenocarcinoma cells and A2780 human ovarian cancer cell line with Ag_5 increased mortality (Figure 2f) (see Figure S23a, Supporting Information). Consistent with cell death being mediated through thiol oxidation by Ag_5, this toxic effect could be abrogated by the thiol-reducing agents, dithiothreitol (DTT) and *N*-acetylcysteine (NAC)[25] (Figure 2f). These results were corroborated in various human cancer cell lines (see Figure S23a–e, Supporting Information).

To further implicate the GSH/GR system in the intracellular catalytic activity of Ag_5, we treated A549 and A2780 cells with various chemicals known to inhibit GSH synthesis. Buthionine-[*S,R*]-sulfoximine (BSO),[26] erastin,[27] and sulfasalazine (SSZ)[28] increased Ag_5 cytotoxicity (see Figure S24a–d, Supporting Information). Erastin and SSZ are pharmacological inhibitors of the cystine transporter SLC7A11, required for GSH synthesis.[27] SLC7A11 expression is enhanced by ARID1A-mediated chromatin remodeling and is frequently mutated in various cancers thus limiting GSH synthesis.[28] Gene silencing of *ARID1A* significantly increases cell sensitivity to Ag_5 (Figure 2g), the estimated ED50 for HCT116 Arid1A$^{(+/+)}$ was 232×10^{-9} M, and for HCT116 Arid1A $^{(-/-)}$ the ED50 value was 192×10^{-9} M. Thus, known *ARID1A* mutations in human cancers may indicate potential for Ag_5 treatment.

Furthermore, PRDX3 oxidation corresponds to cytochrome c release and caspase activation,[29] consequently, we examined the Ag_5 effect on apoptotic biomarkers: PARP cleavage, Annexin-V / FITC and 7AAD staining and caspase-3/7 activation (see Figure S25a,b and Movie S1, Supporting Information). All were activated by Ag_5, indicating Ag_5 is triggering apoptotic cell death and concordant with PRDX3 oxidation. If true, pretreatment with auranofin (AF), a TrxR inhibitor that causes the oxidation of PRDX3[30] could be expected to potentiate Ag_5 cytotoxicity. The combination of AF and Ag_5 present greater cytotoxicity than either treatment alone (see Figure S25c,d, Supporting Information). Conversely, if PRDX3 oxidation is relevant for Ag_5 action, increasing the levels of PRDX3 should reduce Ag_5 efficacy. Transient overexpression of PRDX3 in HEK293 consistently increased the Ag_5 ED50 from 177 ± 12.9 to $193 \pm 14.6 \times 10^{-9}$ M (Figure 2h).

PRDX3 plays an important role in mitochondrial redox control in cancer cells[31] thus, we studied Ag_5 cytotoxicity across a wide range of tumor cell types to see whether it correlates with PRDX3 expression. To this end, an ED50 value for Ag_5 was obtained for each cell line of a panel of 85 human tumor cell lines (see Figure S26, Supporting Information). PRDX3 mRNA levels and ED50 value are inversely correlated (Figure 2i), pinpointing PRDX3 as a primary mediator of Ag_5 action.

2.7. The Cytotoxic Activity of Ag_5 Depends on the Intracellular Redox State

Contingent upon H_2O_2 concentration, Ag_5 catalyzes the irreversible oxidation of GSH and Trx. Thus, we reasoned that cancer cells with an increased generation or reduced disposal of H_2O_2 will be more sensitive to Ag_5. H_2O_2 is generated continuously in cells that consume oxygen and it is well established that during proliferation cell respiration is increased and thus, could be used to target tumor redox vulnerability[32] (see Figure S27a, Supporting Information). Therefore, we explored whether the increased oxidative stress necessary for tumor cell division[33] is sufficient for Ag_5 to trigger cell demise. First, we confirmed that proliferation increased the A549 intracellular oxidative state, assessing the fluorescence due to 2″,7″-dichlorofluorescein (DCF) oxidation, compared

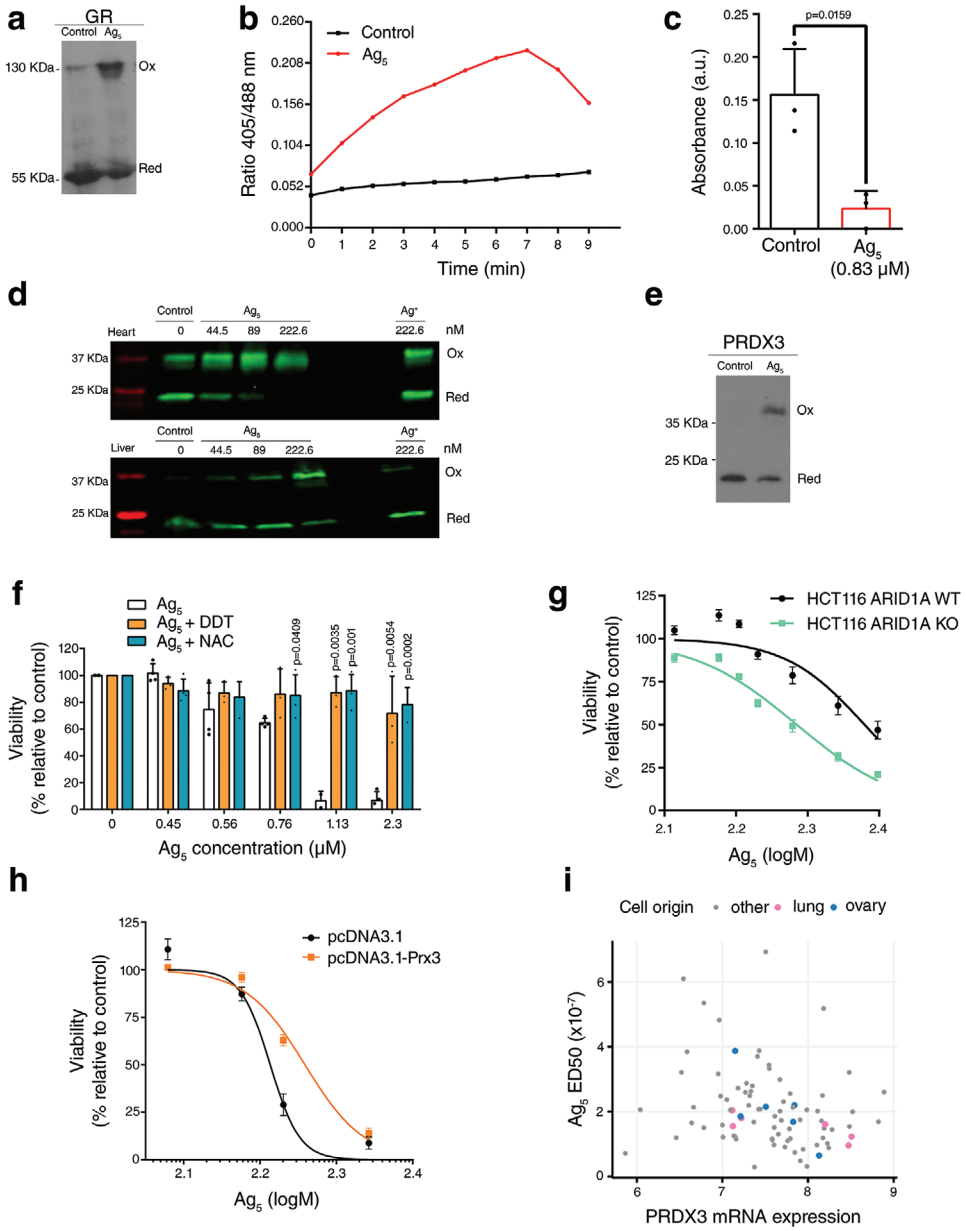

Figure 2. Ag_5 increases intracellular thiol oxidation affecting the Trx and GSH antioxidant systems. a) Western blot analysis showing GR oxidation in A549 cells 15 m after the addition of Ag_5. The results are representative of three independent experiments. b) A549 cells expressing Grx1-roGFP2 were incubated with Ag_5 (0.78×10^{-6} M) analyzed by confocal microscopy. Ratios of the fluorescence excitations at 405/488 nm were recorded for 20 min every 10 s. In each experiment, the ratio was quantified for nine individual cells and plotted against time. Data are representative of three independent experiments. c) Inhibition of the Trx system in the presence of Ag_5. Data are shown as the mean ± SD ($n = 3$), 2-tailed Student's t-test. d) Western blot analysis showing PRDX3 oxidation in mitochondria from the heart (top) and liver (bottom) after Ag_5 (44.5×10^{-9}, 89×10^{-9}, and 222.6×10^{-9} M) and Ag^+ (222.6×10^{-9} M) treatment. The results are representative of three independent experiments. e) Western blot analysis showing PRDX3 oxidation in A549 cells 15 m after the addition of Ag_5. The results are representative of three independent experiments. f) Viability of proliferating A549 cells cotreated with DTT (0.5×10^{-3} M) and Ag_5 ($(0.45–2.3) \times 10^{-6}$ M) for 1 h or pretreated with NAC (5×10^{-3} M) for 1 h and then Ag_5 ($(0.45–2.3) \times 10^{-6}$ M) for an additional 1 h. Data are shown as the mean ± SD ($n = 3$), 2-tailed Student's t-test. g) Viability of HCT116-ARID1A WT and HCT116-ARID1A KO cells treated with Ag_5 ($(0.25–0.13) \times 10^{-6}$ M) for 1 h. Data are shown as the mean ± SD ($n = 3$), 2-tailed paired t-test. $p = 0.0233$. h) Viability of HEK293 cells transfected with pcDNA3.1 empty vector or pcDNA3.1-PRDX3 and treated with Ag_5 ($(0.22–0.12) \times 10^{-6}$ M) for 1 h. Data are shown as the mean ± SD ($n = 3$), 2-tailed paired t-test. $p = 0.0374$. i) Scatterplot of ED50 values measuring sensitivity to Ag_5 versus mRNA expression of PRDX3 for 85 cell lines, Spearman's rank correlation test. $\rho = -0.30$, $p = 0.005$. For all the panels, cell viability was determined by the MTT assay.

to that of nonproliferating A549 cells, consistent with an increased oxidative state (see Figure S27b, Supporting Information). In good agreement, Ag_5 did not affect the viability of confluent non-proliferating cells; however, proliferating A549 cells viability decreased (**Figure 3**a). Likewise, serum starvation, a condition widely used to induce reversible cell

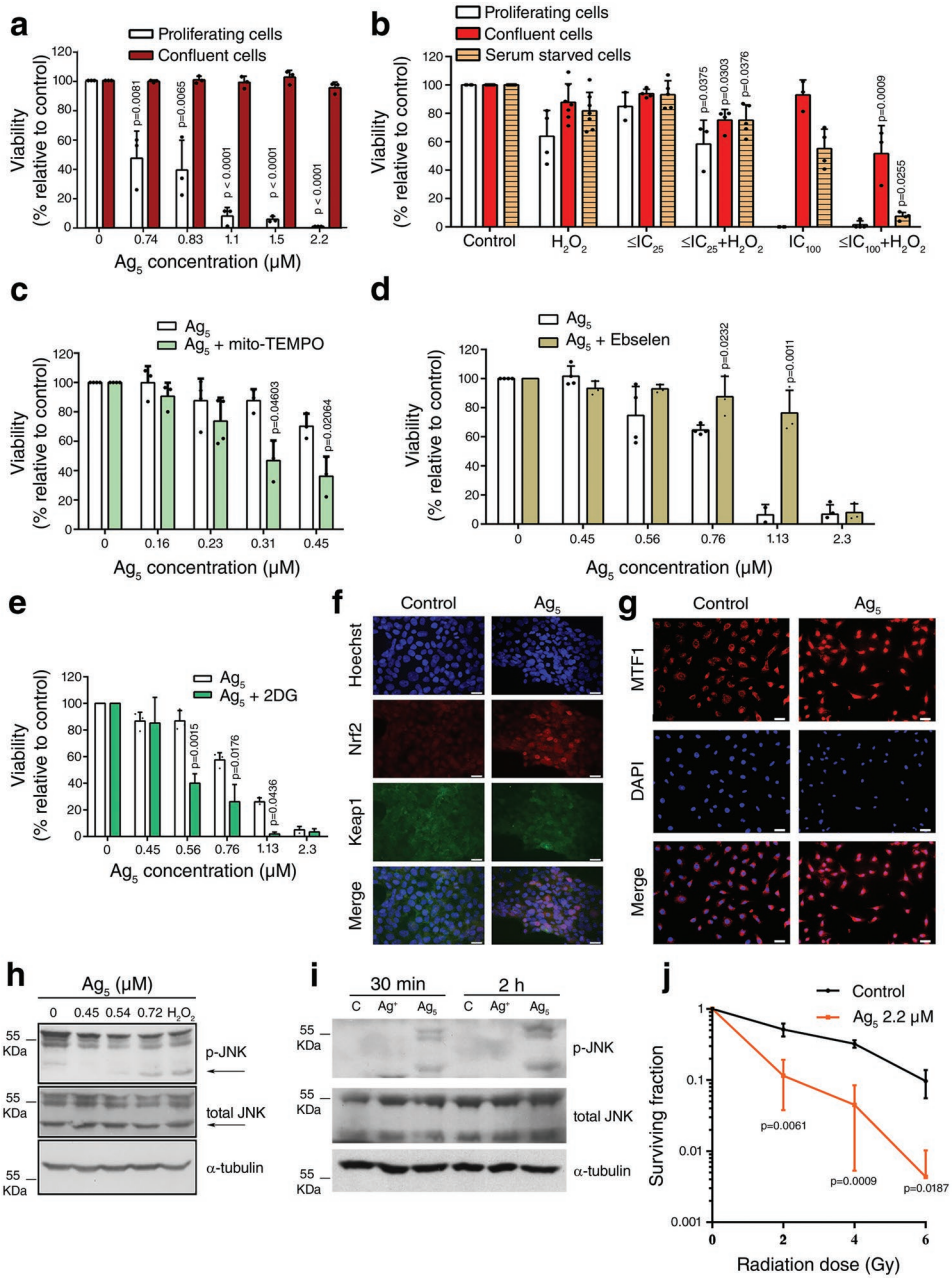

Figure 3. The effects of Ag_5 are dependent on the intracellular redox potential. a) Viability of proliferating and nonproliferating A549 cells exposed to different concentrations of Ag_5 ((0.74–2.2) $\times 10^{-6}$ M). The results are representative of three independent experiments. b) Viability of proliferating and nonproliferating A549 cells treated with Ag_5, H_2O_2, or both. Data are shown as the mean ± SD ($n = 3$), 2-tailed Student's t-test. c) Proliferating A549 cells were treated with mito-TEMPO (20×10^{-6} M) for 1 h and then Ag_5 ((0.16–0.45) $\times 10^{-6}$ M) for 1 h. Data are shown as the mean ± SD ($n = 3$), 2-tailed Student's t-test. d) Proliferating A549 cells were treated with Ebselen (25×10^{-6} M) for 1 h and then treated with Ag_5 ((0.45–2.3) $\times 10^{-6}$ M) for an additional 1 h. Data are shown as the mean ± SD ($n = 3$), 2-tailed Student's t-test. e) Viability of proliferating A549 cells treated with 2DG (20×10^{-3} M) 24 h and then Ag_5 ((0.45–2.3) $\times 10^{-6}$ M) for 1 h. Data are shown as the mean ± SD ($n = 3$), 2-tailed Student's t-test. f) Indirect immunofluorescence images of HEK293T cells stained with an anti-NRF2 antibody (red) and an anti-Keap1 antibody (green). Nuclei were counterstained with Hoechst (blue). Merged images show the nuclear location of NRF2 after 30 min of treatment with Ag_5 (0.52×10^{-6} M). Scale bars 50 μm. g) Indirect immunofluorescence images of A549 cells stained with an anti-MTF1 antibody (red) and counterstained with Hoechst (blue). Merged images show the nuclear location of MTF1 after 2 h of treatment with Ag_5 (0.78×10^{-6} M). Scale bars 50 μm. h) Expression of phospho-Jnk (p-Jnk) and total Jnk in U251 cells treated with Ag_5 (0.45×10^{-6}, 0.54×10^{-6}, and 0.72×10^{-6} M).H_2O_2 (200×10^{-6} M) was used as a positive control, and α-tubulin was used as the loading control. Representative results from three independent experiments are shown. i) Expression of p-Jnk in A2780 cells 30 min and 2 h after Ag_5 (0.1×10^{-6} M) and Ag^+ treatment. Representative results from three independent experiments are shown. j) Survival fraction of A549 cells 8 days after treatment with Ag_5 (2.2×10^{-6} M) and X-ray irradiation (0, 2, 4, and 6 Gy). Data are shown as the mean ± SD ($n = 3$), 2-tailed Student's t-test. For all the panels, cell viability was determined by the MTT assay.

growth arrest (see Figure S27c, Supporting Information), also rendered A549 cells less sensitive to Ag_5. We assumed that Ag_5 has a marked differential effect on proliferating and resting cells due to the displacement of the intracellular redox balance towards an oxidative state brought about by cell division. Corroborating this hypothesis, H_2O_2 administration strongly sensitized both serum-starved and confluent nonproliferating A549 cells to the cytotoxic effect of Ag_5 (Figure 3b). Furthermore, mito-TEMPO, which catalyzes the dismutation of superoxide into H_2O_2 specifically in the mitochondria, increased the cytotoxicity of Ag_5 compared to that with Ag_5 alone in A549 cells (Figure 3c), indicating that mitochondrial H_2O_2 levels are important for Ag_5 activity. Conversely, Ebselen has been reported to decrease ROS levels[34] and it caused a dose-dependent reduction in the cytotoxic effect of Ag_5 on proliferating A549 cells and A2780 cells (see Figure S27d, Supporting Information). To further evaluate the role of the intracellular redox environment in the intracellular catalytic activity of Ag_5, we treated A549 and A2780 cells with 2-deoxyglucose (2DG) that produce oxidative stress[35] and, accordingly increased Ag_5 cytotoxicity (Figure 3e) (see Figure S27e, Supporting Information). Further confirmation of the link between Ag_5 action and the intracellular oxidative state comes from comparing the cell oxidative state, as seen by DCF fluorescence, among the A549 and A2780 cell lines. A2780 cells shown an increased fluorescence and are more sensitive to Ag_5 (see Figure S27f, Supporting Information). In summary, in the presence of an intracellular oxidative environment, Ag_5 accelerates oxidative reactions, leading to programmed cell death. However, in a reductive intracellular environment, Ag_5 has no biological effects.

2.8. Ag_5 Activate Redox Signaling Pathways

Ag_5 mediated oxidation of GR and PRDX3 should lead to oxidative stress and, consequently, activation of redox signaling pathways. Among the most well-known redox signaling pathways are ASK1,[36] NRF2-KEAP1,[37] and MTF1[38] pathways. NRF2 and MTF1 are nucleocytoplasmic shuttling proteins that accumulate in the nucleus upon activation. In the presence of Ag_5, we observed the nuclear accumulation of NRF2 (Figure 3f) (see Figure S28a,b, Supporting Information) and MTF1 (Figure 3f) (see Figure S28c, Supporting Information). Confirming previous findings, we observed a significative reduction in the nuclear accumulation of MTF-1 and NRF2 in HEK293T cells treated with Ag_5 in the presence of DTT (0.5×10^{-3} M) (see Figure S28b,c, Supporting Information). Moreover, qPCR confirmed the overexpression of genes under NRF2 transcriptional regulation, *HMOX1* and *GCLM*, and genes transcriptional regulated by MTF-1, *MT1F* and *MT1X* in a human multiple myeloma MM.1S cell line (Table S3, Supporting Information). Furthermore, activation of the ASK1 pathway was assessed by analyzing its downstream effector c-Jun N-terminal kinase (JNK).[39] Ag_5 treatment caused a dose- and time-dependent increase in JNK phosphorylation, indicating ASK1 activation (Figure 3h,i, respectively). JNK phosphorylation activates mitochondrial death factors such as Bim and Bax, resulting in cytochrome c release and initiation of apoptosis[40] suggesting that various effectors can mediate apoptosis triggered by Ag_5.

2.9. X-Ray Irradiation Enhances the Intracellular Catalytic Activity of Ag_5

Radiotherapy forms free radicals, notably OH•, which then damages the DNA. XANES experiments suggested that the increase of OH• in irradiated cells could sensitize them to Ag_5. Of relevance, Ag_5, in combination with X-ray irradiation at even at the lowest absorbed dose, 2 Gy, decreased cell viability, indicating X-ray irradiation cooperates to increase Ag_5 cytotoxicity (Figure 3j) (see Figure S29a, Supporting Information). Importantly, X-ray irradiation-induced potentiation of the effect of Ag_5 on cell death was not due to a concomitant increase in phosphorylation of the histone H2AX (γ–H2AX), a marker for DNA damage (see Figure S29b, Supporting Information), suggesting that Ag_5 acts through a different cell death mechanism, probably using OH• generated by X death-ray irradiation to accelerate irreversible Cys oxidation, as XANES experiments suggests.

2.10. Ag_5 Preferentially Cause Cell Death in RAS-Transformed Cells and Hypoxic Cells

Activated oncogenes cause metabolic changes that give rise to the accumulation of ROS.[41–43] We therefore reasoned that compared to non-transformed cells, transformed cells would be preferentially killed by treatment with Ag_5. To evaluate this hypothesis, we introduced a doxycycline-inducible activated allele of *HRAS* ($HRAS^{G12V}$) into non-transformed immortalized mouse fibroblasts (W3T3 cells) and confirmed inducible *HRAS* expression by western blotting (**Figure 4**a). Interestingly, cells expressing *HRAS* had greater DCF fluorescence, indicating increased oxidation (Figure 4b) and were more sensitive to cell death induced by Ag_5 activity than noninduced cells (Figure 4c). These effects were inhibited by DTT coadministration, confirming that *HRAS*-induced redox changes are responsible for the increased effects of Ag_5 (see Figure S30, Supporting Information).

Metabolic phenotypes in tumors are both heterogeneous and flexible[44,45] and thus may affect Ag_5 therapeutic efficacy. Conditions within tumoroids or multicellular tumor spheroids (MCTSs) resemble the pathophysiological conditions within human tumor tissue in many ways and are widely used for drug testing.[46] Like human tumors, large MCTSs, more than 600 μm diameter, are characterized by a heterogeneous cell subpopulation, with actively proliferating cells on the periphery and quiescent, hypoxic, and necrotic cells in the inner regions.[47] Therefore, to assess the effects of the Ag_5 on hypoxic cells, we developed A549 cell MCTSs as an ex vivo tumor model. The MCTSs were treated with Ag_5 (4.5×10^{-6} M) four times (days 0, 2, 4, and 6, with the first day of treatment set as day 0) or vehicle (control) and examined daily. Ag_5 treatment decreased the area of the MCTSs over the seven-day period (see Figure S31, Supporting Information). Notably, a less dense region was observed in the center of the MCTSs treated with Ag_5, but not the control MCTSs, suggesting decreased cellularity that appears to be more pronounced in hypoxic centrally located cells of the MCTSs (Figure 4d, red arrow). Comparable results were obtained in MCTSs formed from HCT116,

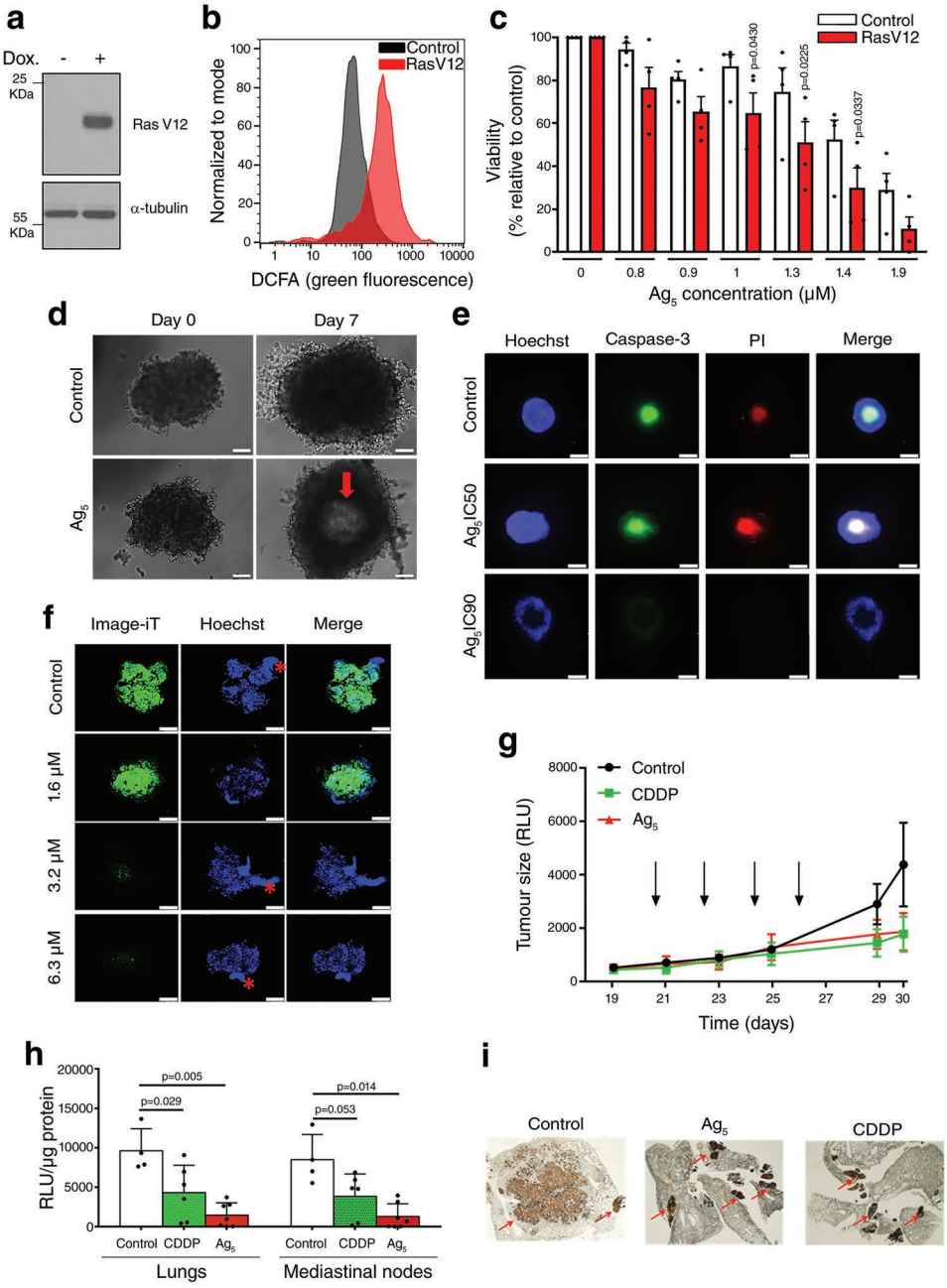

Figure 4. Ag_5 preferentially induce cell death in RAS-transformed and hypoxic cells and show antitumoral activity in vivo. a) W3T3 cells carrying a doxycycline inducible RASV12 allele were exposed to doxycycline (red bars) or vehicle (white bars) for 24 h and then treated with different concentrations of Ag_5 (2.6–7.5 × 10^{-6} M). RASV12 expression was assessed by western blotting, b) DCFA oxidation induction was measured by flow cytometry, and c) cell viability was determined by MTT assay 24 h later. Data are the mean ± SEM of four independent experiments: two-way ANOVA with Bonferroni's correction. d) Images of control and Ag_5-treated MCTSs formed from A549 cells showing differences in size and cellular density in the central region (red arrows). Scale bar 100 × 10^{-6} M. e) Optical sections of live HCT116 cell-derived MCTSs treated with Ag_5 obtained with light sheet fluorescence microscopy (LSFM). Nuclei were stained using Hoechst, dead cells using propidium iodide (PI) and apoptotic cells using the CellEvent Caspase-3/7 green detection reagent. Scale bar 200 × 10^{-6} M. f) Confocal images of live A549 cell derived MCTSs treated with Ag_5. Hypoxic regions were stained using Image-iT green hypoxia reagent. Nuclei were stained by Hoechst. Red asterisks point to agarose that remained adhered to the spheroid surface. Scale bar 200 × 10^{-6} M. g) Tumor growth in mice with orthotopic lung cancer was measured in vivo by luminescence (IVIS Spectrum). Black arrows indicate days on which treatments were administered. h) Luciferase activity was quantified ex vivo in lung and mediastinal lymph nodes. i) Immunohistochemical staining of lung tumors with a monoclonal antibody specific for human cytokeratin 7 allowed us to differentiate the morphology of the tumor and nontumor tissues. Red arrows indicate tumor nodules. Experimental groups: CDDP (4 mg kg^{-1}), Ag_5 (0.25 mg kg^{-1}), and control (no treatment). Data represents the mean ± SD. Error bars represent standard deviation; n = 5 mice per group. Mann-Whitney test.

indicating that cellular distribution rather than the cell line, was responsible for the effect (Figure 4e). The presence of these Ag_5 sensitive inner regions in the MCTSs after Ag_5 treatment could be related to the ability of the Ag_5, given their small size and neutral charge, to penetrate the MCTSs and reach these central hypoxic regions commonly found in human tumors.[48]

Then, because both hypoxia and low-glucose conditions increase intracellular oxidation,[33] we hypothesized that they would sensitize cells to Ag_5 activity. To assess this hypothesis, we first measured the degree of hypoxia in the tumoroids using a fluorescent probe to confirm the presence of hypoxic conditions and clearly observed in a 1000-cell tumoroid (Figure 4f, top row). Interestingly, exposure of the tumoroids to Ag_5 at increasing doses caused a dose-dependent reduction in hypoxic cells (Figure 4f). Nevertheless, a fraction of the cells in the tumoroid is resistant to Ag_5, which we tentatively ascribed to nonproliferating cells with a higher intracellular reductive state; further characterization is now needed to establish whether cellular resistance is permanent or can be reversed when cells proliferate again.

2.11. Ag_5 Show Antitumoral Activity In Vivo

To determine whether the in vitro results described above would be confirmed through in vivo experiments, we evaluated the anti-tumoral activity of Ag_5 in vivo by using an orthotopic model of metastatic lung cancer[49] in which metastatic cells can be detected in the mediastinal lymph nodes 13 days after the injection of cancer cells into the lung. Therefore, to evaluate the effects of Ag_5 on an advanced cancer in which metastasis has occurred, we intravenously administered Ag_5 20 days after the implantation of cancer cells in the lung, when lymph node metastases were already evident. Tumor growth was measured over time by in vivo bioluminescence imaging, and the cancer cell burden from both lymph node metastases and the primary tumor was assessed ex vivo at the time of sacrifice. Cisplatin (CDDP), a first-line treatment for metastatic lung cancer, was used as positive control for tumor growth inhibition. As shown in Figure 4g, treatment with Ag_5 significantly reduced tumor growth compared to that in untreated animals, in which the tumors grew exponentially. Additionally, compared to control mice, Ag_5-treated mice exhibited significantly reduced luciferase activity in both the primary tumor and mediastinal lymph nodes at the time of sacrifice (Figure 4h). Further immunohistochemical analysis of lung sections from the mice confirmed the antitumor effect of Ag_5 (Figure 4i). Additionally, no signs of toxicity, either by body weight loss or by blood cell counts, were observed in the mice after treatment with Ag_5 at the therapeutic doses used, suggesting their potential safety in humans (Table S4 and Figure S32, Supporting Information). Together, these results show the ability of Ag_5 to significantly decrease both the primary tumor and metastatic cell burden in an advanced metastatic cancer.

3. Conclusion

There are very few redox active therapeutic modalities. Here we have shown that the unique intracellular chemistry of Ag_5 can selectively target and disrupt cell metabolism in cells with elevated redox stress, such as cancer cells. Treating tumors based on their unique genetic profile has proved difficult, exposed the patients to severe toxicity when either monotherapy or combination therapy has been used, and acquired resistance is common.[50] As an alternative, targeting metabolic vulnerabilities shared by tumors has generated growing interest in recent years. Here we show that Ag_5 triggers tumor cell death by acting synergistically with the elevated levels of redox stress in tumor cells. Importantly, in most normal resting cells which have a low level of redox stress, so H_2O_2 levels are low, while the oxidation of their thiols is accelerated by Ag_5, the unstressed antioxidant systems in these cells can maintain homeostasis. However, if H_2O_2 levels increase above a threshold level, for example in tumors, antioxidant systems are overwhelmed because they cannot counteract the increased oxidation rate caused by the presence of Ag_5. Also, if the antioxidant systems are affected, the necessary amount of H_2O_2 to produce cell death in the presence of Ag_5 is lower. Therefore, Ag_5 does not induce cell death in the balanced redox environment in normal cells, but when the redox balance is skewed in the presence of elevated intracellular H_2O_2 production, Ag_5 can catalyze the irreversible oxidation of thiol groups in key molecules of both the GSH and Trx antioxidant pathways, particularly in the mitochondria that ultimately leads to oxidative stress and cell death. Of relevance, our results indicate that X-ray irradiation forming free radicals sensitized cells to Ag_5; the combination of Ag_5 with X-ray irradiation, at even at the lowest absorbed dose, improves the therapeutic ratio of radiation, which now deserves further studies.

Hypoxia is strongly associated with poor prognosis[51] and is a leading cause of therapy resistance,[52] the finding that Ag_5 was effective in reducing hypoxic regions of MCTS is of interest as a potential new approach for the treatment of tumor hypoxic cells. Therapeutic efficacy of Ag_5 was demonstrated in an orthotopic model of metastatic lung cancer in which Ag_5 was shown to inhibit the growth of both the primary tumor and the mediastinal lymph node metastases. These findings are of particular interest because high ROS levels have not only been described in proliferating tumor cells, but also in metastatic settings. Our findings suggest the unique intracellular redox chemistry of quantum clusters may lead to new redox-based approaches to cancer therapy.

4. Experimental Section

Synthesis of Ag Clusters: Unless otherwise specified, all reagents were purchased from Sigma Aldrich, Co., Spain. Thioredoxin (TRX-01 Thioredoxin1, *E. coli* (native)) was purchased from IMCO Corp Ltd AB. Silver sheets (99%) were purchased from Goodfellow Cambridge Ltd., Huntingdon, UK. Alumina nanoparticles (average size ≈ 50 nm) and cloth pads were purchased from Buehler, Düsseldorf, Germany.

Sandpaper (1000 grit) was supplied by Wolfcraft España S.L, Madrid, Spain. All aqueous solutions were prepared with MilliQ-grade water using a Direct-Q8UV system from Millipore (Millipore Ibérica S.A., Madrid, Spain). Mica sheets (Grade V-1 Muscovite) were purchased from SPI Supplies, West Chester, PA, USA.

The synthesis was carried out with a Biologic VMP300 potentiostat (Seyssinet-Pariset, France). A Methrom thermally insulated three-electrode electrochemical cell, deoxygenated just prior to the synthesis, was used with a hydrogen electrode as a reference and two Ag foils (17.5 cm^2 surface

area) as counter and working electrodes. The experimental conditions were similar to those reported before,[14,15] but the voltage was increased with respect to the preparation of Ag_3 clusters (10 V) because in this way larger clusters are produced. This (besides the electrode's polishing, which determines the surface's roughness) is crucial for achieving the desired cluster's size, as it will be reported elsewhere. It has to be noted that Ag clusters with larger sizes were also synthesized (mainly consisting in Ag_7 and Ag_9, see inset in Figure S4, Supporting Information) increasing further the voltage, to compare their biological properties with the ones reported here. Prior to the synthesis, both silver electrodes were polished with sandpaper followed by alumina (≈50 nm), washed thoroughly with MilliQ water and sonicated. An ion-selective electrode was used to verify that, after synthesis, the concentration of remaining Ag^+ ions are always less than 3 mg L^{-1} after precipitation with NaCl, and various techniques were used to characterize the synthesized Ag clusters (see also below). The samples were finally concentrated at 50 °C using a rotary evaporator (Buchi Rotavapor R-210 at a pressure of 2 mbar) (Massó Analítica S.A., Barcelona, Spain) to a final concentration of ≈30 mg L^{-1} as determined by flame atomic absorption spectroscopy.

Cluster's Characterization Methods: In Ag clusters' characterization methods, both UV–vis and fluorescence spectroscopy experiments were performed at room temperature using 1 cm path length Hellma quartz cuvettes (Hellma GmbH & Co. KG., Müllheim, Germany). UV–vis spectra were recorded with an Analytik Jena Specord S600 spectrometer (Analytik Jena AG, Jena, Germany) with a diode array detector, and fluorescence spectra were recorded with a Cary Eclipse Varian fluorimeter (Agilent Technologies Spain, S.L., Madrid, Spain).

Electron microscopy studies were performed on a FEI Titan Themis 60-300 Double Aberration Corrected microscope operated at 200 kV. The aberrations of the condenser lenses were corrected up to fourth order using the Zemlin tableau to obtain a sub-Angstrom electron probe. A condenser aperture of 50 µm yielding an electron probe with a convergence angle of 20 mrad was used. To avoid sample modification under the electron probe a beam current of 0.025 nA was used. STEM samples were prepared by depositing one drop of Ag clusters' solution onto holey carbon coated Cu grids. After preparation, samples were maintained under vacuum conditions.

Electrospray ionization time-of flight (ESI-TOF) mass spectrometry measurements were performed using a Bruker MicroTOF mass-spectrometer operating in negative ionization mode. Temperature control and nitrogen drying gas (1 µL/144 min) in ESI source were employed to assist the ionization process. The ESI source conditions were as follows: source voltage –4.5 kV, heated capillary temperature 275 °C, capillary voltage –35 V and sheath gas and auxiliary gas 5 and 2 (N_2, arbitrary units). For full-scan MS analysis, the spectra were recorded in the range of m/z 100 to 1000 with a scan speed of 1 scan/s. All spectra were acquired in reflectron mode of the TOF mass spectrometer equipped with multistep detection to obtain maximum sensitivity. The mass resolution was set at 15000 FWHM. The instrument was calibrated using a calibration solution according to the manufacturer's instructions. Due to the difficulty to charge the uncharged clusters[15] a systematic investigation was carried out to obtain the maximum sensitivity for the detection of Ag clusters. As it will be published elsewhere, concentrations of NaCl and formic acid are crucial to achieve this, approaching 0.1 ppm sensitivity for the optimal conditions. 2 µL of Ag clusters' solutions diluted 300 times to contain 25×10^{-3} M of NaCl (which is the optimum NaCl concentration for Ag clusters' detection) was directly injected into a mobile phase of acetonitrile containing 0.1% formic acid at a flow rate of 0.2 mL min^{-1}. Details of the analysis of Ag clusters' peaks are given in the Supporting Information.

Ion concentration was measured using a previously calibrated pH and Ion-Meter GLP 22 (Crison Instruments S.A., Barcelona, Spain) by adding a stabilizing solution ($NaNO_3$ 5 M) at a ratio of 2:100 to the sample at a constant temperature of 25 °C.

The total Ag content in the clusters' samples was analyzed by flame atomic absorption spectroscopy, performed with a PerkinElmer 3110 with an Ag hollow cathode lamp Lumia from PerkinElmer (Madrid, Spain) (current 10 mA).

XANES Characterization of Sulfur Oxidation States: S K-edge (2470 eV) and L3 Ag-edge (3351 eV) X-ray absorption near edge structure (XANES) experiments were performed at de SXS beamline at the Laboratório Nacional de Luz Síncrotron (LNLS, Campinas, Brazil) which was equipped with an InSb (111) double crystal monochromator with slit aperture of 1 mm, to achieve a resolution of about 0.5 eV. Details of the experimental setup of the SXS beam line were published elsewhere.[53] X-ray absorption spectra were recorded in fluorescence mode, collecting the emitted X-ray from the S K$\alpha_{1,2}$ (at 2309.5 and 2308.4 eV, respectively) and Ag Lα_1 (at 2982.7 eV) emission lines for each measured edge. Absorption experiments were performed either in a vacuum of 10^{-8} mbar at room temperature, and in a special liquid sample holder designed ad hoc for the experiment with reactive oxygen species, at room temperature and atmospheric pressure, allowing us to determinate initial reactions intermediaries as well as final compounds. The photon energy was calibrated by assigning the value 2481.5 eV to the highest maximum of $Na_2S_2O_3$ (corresponding to the so-called inner sphere), in accordance with the criteria previously reported by Vairavamurthy.[54] The final XANES spectra were obtained after background subtraction and normalization to the post edge intensity, following usual procedure described elsewhere. XANES quantification were performed with Athena software and subsequent analysis on Origin lab software. For GSH characterization, a fraction of solution was deposited by drop casting on carbon disks (Ted Pella, Inc) to have an Ag or S concentration in a detectable value. For Trx samples, they were carefully mounted in a liquid sample holder, designed ad hoc for this experiment. Phosphate buffered saline (PBS) solution was used as the solvent in all the reaction mixes with Trx, with the purpose to reproduce the same intracellular pH and ionic strength. The hydroxyl radical solutions were prepared by Fenton reaction, with H_2O_2 and $FeCl_2$. Concentration values are indicated in the Table S1, Supporting Information.

Theoretical Calculations: DFT and QM/MM calculations were performed on the systems shown in the Supporting Information, with full geometry optimization, using the B3LYP[55,56] functional, the 6-31G(d,p)[57,58] basis set for H, C, N, O, S atoms, and Lanl2dz[59] basis set for Ag. The ONIOM[60] method was used for two layers QM/MM calculations and the UFF[61] force field was used in the lower layer. The implicit water solvent was considered through the C-PCM[62] method. Transition state structures were found by using the synchronous transit guided quasi-Newton method.[63] Frequency calculations, within the harmonic oscillator approximation, were performed on the optimized geometries, to confirm that they corresponded to minimum energy structures (all real vibration frequencies) or transition states (one imaginary vibration frequency). All calculations were performed by the Gaussian09[64] program package.

Ag_5 Biological Action: The following reagents were used: 3-(4,5-dimethyl-2-thiazolyl)-2,5-diphenyl-2*H*-tetrazolium bromide, MTT (Sigma, M2128), hydrogen peroxide solution, H_2O_2 (Sigma, 516813), DL-dithiothreitol (DTT) (Fluka, 43815), 2-deoxi-D-glucose, 2DG (Sigma, D6134), L-buthionine-sulfoximine, BSO (Sigma, B2515), *N*-acetyl-L-cysteine, NAC (Sigma, A9165), Erastin (Sigma, E7781-5MG), Sulfasalazine (Sigma, S0883-10G) Ebselen (Enzo, ALX-270-097-M005), Auranofin (Sigma, A6733) CM-H_2DCFDA (Molecular Probes, C6827), CellEvent Caspase 3/7 Reagent (Molecular Probes, C-10423), Annexin V-FITC (BD Pharmingen, 550911), 7-amino actinomycin D, 7-AAD (Molecular Probes, 00-6993-50) β-nicotinamide adenine dinucleotide reduced disodium salt hydrate, NADH (Sigma, N8129), doxycycline hyclate (Sigma, D9891), biotin ethylenediamide iodoacetamide (biotium, 90059), β-nicotinamide adenine dinucleotide 2′-phosphate reduced tetrasodium salt hydrate, NADPH (Sigma, N7505), seleno-L-cystine (Sigma, 545996), Insulin from bovine pancreas (Sigma, I1882), Rat recombinant Thioredoxin Reductase 1 (IMCO, TR-03) Image-iT Green Hypoxia Reagent (Molecular Probes, I14834), Premo Cellular Redox Sensor Grx-1-roGFP (Molecular probes, P23648), Hoechst 33258 (Molecular Probes, 10778843), Fluoroshield Mounting Medium (Sigma, F6182), The following antibodies were used: anti-phospho-histone H2AX (Ser 139) FITC conjugate (Millipore, 16-202A), anti-MTF-1 (Santa Cruz Biotechnology, sc-48775), anti-Nrf2 (Santa Cruz Biotechnology,

sc-722), anti-Keap 1 (Santa Cruz Biotechnology, sc-15246), anti-PRDX3· (Abcam, ab73349), anti-GR (Santa Cruz Biotechnology, sc-133245) anti-pSAPK/JNK Thr183/Tyr185 (Cell Signaling, 9251), anti-total JNK1/3 (Cell Signaling, 9252), anti-Pan-Ras (Merck-Millipore, OP40), anti-cleaved PARP Asp214 (Cell Signalling, 5625), anti-α-tubulin (Sigma, T9026) primary antibodies; Alexa Fluor-594 goat anti-rabbit IgG (Life Technologies, A-11012), Alexa Fluor-488 donkey anti-goat IgG (Life Technologies, A-11055), anti-mouse IgG-HRP (GE Healthcare, NA931), anti-rabbit IgG-HRP (GE Healthcare, NA934) and IRDye 800CW Goat anti-Rabbit IgG (Licor, 926-32211) secondary antibodies. The following TaqMan Gene Expression Assays (ThermoFisher) were used: HMOX1 (Hs01110250_m1), GCLM (Hs00157694_m1) MT1F (Hs00744661_sH) and MT1X (Hs00745167_sH).

Animals: All mice research in this study was done in accordance with Spanish and European regulations and approved by the USC Ethics Committee (project ID 15010/14/001). The orthotopic lung cancer model was generated by injection of luciferase-expressing A549 cells into the left lung of nude mice essentially as described.[14,49] Tumor-bearing animals were treated with cisplatin (four doses, 4 mg kg^{-1}), Ag_5 (four doses, 0.25 mg kg^{-1}) or left untreated (control group). Treatments were administered intravenously. In vivo tumor evolution was followed by bioluminescence in anesthetized mice using an IVIS Spectrum Image System (Perkin Elmer). Upon sacrifice ex vivo luminescence and histological analysis were performed as described previously.[14]

In histological analysis, lungs were fixed in 10% neutral buffered formalin for 24 h and embedded in paraffin. Sections 4 mm thick were mounted on FLEX IHC microscope slides (Dako-Agilent, Glostrup, Denmark) and heated at 60 °C for 1 h. The immunohistochemical technique was automatically performed using an AutostainerLink 48 (Dako-Agilent). After deparaffination and epitope retrieval in EnVision FLEX target retrieval solution (high pH) for 20 min at 97 °C, the slides were allowed to cool in PT Link to 65 °C and then in Dako wash buffer for 5 min at room temperature. The immunostaining protocol included incubation at room temperature in: 1) EnVision FLEX peroxidase-blocking reagent (Dako-Agilent) for 5 min; 2) ready-to-use FLEX primary antibody (Dako-Agilent) anti-CK7 (clone OV- TL 12/30), for 20 min; 3) EnVision FLEX/HRP (dextran polymer conjugated with horseradish peroxidase and affinity-isolated goat antimouse and antirabbit immunoglobulins) for 20 min; 4) substrate working solution (mix) (3,3′-diaminobenzidine tetrahydrochloride chromogen solution) (Dako-Agilent) for 10 min; and 5) EnVision FLEX hematoxylin (Dako- Agilent) for 9 min. Sections were examined and photographed using an Olympus PROVIS AX70microscope equipped with an Olympus DP70 camera.

All rats' experiments were carried out in accordance with the UK Animals (Scientific Procedures) Act of 1986 and the University of Cambridge Animal Welfare Policy. Wistar rats (003, wildtype, female) were ordered from Charles River Laboratories UK (Margate, UK). They were housed under standard laboratory conditions with ad lib food and water and used between 10 and 12 weeks. Animals were culled by cervical dislocation with accordance to UK Home Office Schedule 1.

A549 and MCF7 cells were obtained from the Deutsche Sammlung von Mikroorganismen und Zellkulturen (DSMZ). A549-Luc were obtained from Caliper. HCT116 ARID1A-KO (Q456X/Q456X) and parental were purchased from Horizon Discovery. MM.1S, MOLT-4, K-562, U-87 MG, and HEK293 cells were obtained from the ATCC. U251-Luc cells were kindly provided by Dr. J Seoane (Vall d´Hebron Institute of Oncology). A549, A549-Luc, U251-Luc, A2780, W3T3 RasV12, and HEK293 cell lines were maintained in DMEM-low glucose (D6046, Sigma); MCF7 and U87 cell lines in DMEM-high glucose (D5671,Sigma); HCT116, HCT116 ARID1A-KO, MM1S, K562, and MOLT-4 in RPMI 1640 (R-5886, Sigma), modified cell lines (A549-Luc and U251-Luc) were supplemented with puromycin (1.3 µg mL^{-1}) to select the stable transfected cells. For Ras expression, W3T3 cells were infected with the pInducer20 HRASV12 lentiviral vector and cultured in the presence of 6 µg mL^{-1} doxycycline. All cell lines were cultured at 37 °C in a humidified atmosphere in the presence of 5% CO_2 and 95% air. Cells were routinely tested negative for mycoplasma contamination. Unless otherwise specified Ag_5 treatment was done in complete culture medium without FBS.

Screening of the cell panel was carried out by OncoLead (OncoLead GmbH & Co. KG, Zugspitzstr. 5, 85757 Karlsfeld, Germany).

Mammalian Mitochondrial Preparations: Mitochondria isolation from rat liver and rat heart was prepared as described previously.[8] Bovine heart mitochondrial membranes (BHM) were prepared as described previously.[65,66] Protein concentration was determined using the bicinchoninic acid (BCA) assay with BSA as a standard.

Ag_5 Uptake: Cellular uptake: MOLT-4 (6×10^6) cells were incubated with Ag_5 (557×10^{-12} M) for 5 min at 37 or 4 °C. After that, cells were centrifuged for 5 min at 1000 rpm. Supernatant was collected, and cellular pellet was washed with cold PBS and centrifuged at 4 °C for 5 min at 1000 rpm.

Mitochondrial uptake: 1 mg mL^{-1} of isolated mitochondria from rat liver were incubated for 5 min at 37 °C with Ag_5 (333×10^{-9} M) and either rotenone (4 µg mL^{-1}); rotenone (4 µg mL^{-1}) and succinate (5×10^{-3} M); rotenone 4 (µg mL^{-1}), succinate (5×10^{-3} M), and carbonyl cyanide 4-(trifluoromethoxy)phenylhydrazone (FCCP) (500×10^{-9} M). Alternatively, FCCP was added after the incubation with the previous mixture. Then, mitochondria were centrifuged at full speed for 1 min and pellet was collected.

Both, cellular and the mitochondrial pellets were digested in HNO_3 at 90 °C for 4 h. Ag concentration was measured in a NexION 300X ICP-MS, Perkin Elmer.

Cell Viability Assays: Cells were seeded in a 96-well plate [A549 (4×10^3 cells per well), MCF7 (4×10^3 cells per well), U87-Luc (5×10^3 cells per well), HCT116 (5×10^3 cells per well), HEK293 (5×10^3 cells per well), and A2780 (6×10^3 cells per well)]. For proliferating cells, 24 h later cells were treated under different conditions: 1) with Ag_5 at the desired concentrations for 1 h, 2) with H_2O_2 (200×10^{-6} M) alone or in combination with Ag_5 for 1 h, 3) preincubated with NAC (5×10^{-3} M) or Ebselen (25 µL) for 1 h or with 2DG (20×10^{-3} M) or BSO (20×10^{-3} M) for 24 h and then treated with Ag_5 at desired concentrations for 1 h more, and 4) treated with DTT (0.5×10^{-3} M) alone or with Ag_5 and DTT (0.5×10^{-3} M) for 1 h. Then, the medium was replaced with complete medium for 24 h more and cell death was measured by the MTT assay. 10 µL of MTT solution (5 mg mL^{-1}) were added to each well and incubated at 37 °C protected from light. 4 h later, 100 µL of solubilization solution (SDS/0.1N HCl) were added and samples were incubated for 18 h at 37 °C. Absorbance was measured at 595 nm using a CLARIOstar microplate reader. For nonproliferating cells, proliferation was stopped using two approximations: 1) confluency: cells were allowed to grow during 96 h in medium-10% of FBS to reach the confluence and 2) serum starvation: 24 h after seeding medium was replaced with medium-0.05% of FBS for 72 h. Then, cells were treated with 1) Ag_5 for 1 h and incubated in complete medium for 24 h more or 2) with H_2O_2 (200×10^{-6} M) alone or in combination with Ag_5 for 1 h. Then, the medium was replaced with complete medium for 24 h more and cell death was measured by the MTT assay as described above.

Trx and TrxR Activity: Trx and TrxR activity was assessed using the Kit for assays of mammalian Trx and TrxR (IMCO) following manufacturer's instructions.

To measure Trx activity, Trx and TrxR were incubated with different doses of Ag_5 for 30 min following manufacturer's instructions. Then, absorbance was measured at 412 nm using a CLARIOstar plate reader, BMG Labtech. The effect of Ag_5 in Trx activity was determined by the inhibition of TNB signal.

TrxR activity was measured using two electron acceptors: 1) Selenocysteine (protocol adapted from Cuniff et al.[67]). TrxR from rat liver (100 ng dissolved in PBS) was incubated with Ag_5 (1.13×10^{-6} M) or Ag^+ (at the same Ag concentration) for 10 min in a 96-well plate. After that, a solution of NADPH and Selenocysteine was added to each well at a final concentration of 400×10^{-6} M. Immediately, NADPH consumption was measured at 340 nm for 30 min using a SpectraMax platereader, Molecular Devices. 2) H_2O_2 (protocol adapted from Zhao et al.[68]). TrxR from rat liver (17×10^{-9} M, dissolved in Tris–Cl pH 7.5 50×10^{-3} M, EDTA 1×10^{-3} M) was incubated for 30 min with Ag_5 (1.15×10^{-6} M) in a 96-well plate. Then, H_2O_2 (0.5, 1, 2, and 5×10^{-3} M) was added. Finally, NADPH (dissolved in Tris 50×10^{-3} M, EDTA 1×10^{-3} M) was added to each well

at a final concentration of 100×10^{-6} M. Immediately, the plate was read at 340 nm in a CLARIOstar platereader, BMG Labtech.

Insulin Oxidation: For the aerobic conditions, 210×10^{-3} M HEPES pH 7.6, 790×10^{-6} M insulin and 20×10^{-3} M EDTA were mixed and 19.2 µL of the solution were incubated in TE buffer with 5 µL of 0.5 M DTT and 5 µL of 12.3×10^{-6} M Ag_5 as indicated in 50 µL final volume for 30 min. Then, 200 µL of 1×10^{-3} M DTNB supplemented with 7.2 M GuHCl in 0.18 M Tris–Cl pH 8.0 and 9.95% ethanol was added to each well and absorbance was measured at 412 nm using a micro plate reader in a CLARIOstar platereader, BMG Labtech.

For the anaerobic conditions, insulin was incubated in TE buffer and DTT as described above in a Baker Ruskinn Invivo2 200 hypoxic chamber (0.2% O_2 and 5% CO_2) prior deoxygenation of samples for 30 min. Then, insulin sample was tested in the presence of DTT (control) or passed through a Illustra MicroSpin G-25 Column, GE Healthcare containing Sephadex as manufacturer's instructions to remove DTT. After that, 5 µL of deoxygenated Ag_5 (9.6×10^{-6} M) were added and after a 30 min incubation in hypoxic conditions, DTNB was incorporated and absorbance was measured as described above.

GSH Oxidation in Living Cells: A549 cells (2.5×10^4 cells) were seeded in 35 mm plate dishes (Mattek) and transduced with the Premo Cellular Redox Sensor Grx-1-roGFP following manufacturer's instructions. After that, Ag_5 (IC_{50}) were added to the dish and cells imaged during 10 min. Images were taken every 10 s using a Leica TCS SP8 confocal microscope. Fluorescence intensity emitted by each cell was measured at 405 and 488 nm and emission was collected at 500–530 nm to calculate the ratio 405/488. Images were processed using the ImageJ software. Ratio images were created using the RatioPlus Plugging and the ImageJ Look Up table "green fire blue" was used to create false-color ratio images.

GSH/GSSG Ratio: A549 cells (6×10^3 cells) were seeded in 96-well clear bottom white microplates and 24 h later treated with Ag_5 (IC_{50}) for 1 h. Then, oxidized, and total glutathione were measured using the GSH/GSSG-Glo Assay according to the instructions of the kit using a CLARIOstar microplate reader.

PRDX3 Transfection: HEK293 cells were transfected with pcDNA3.1-PRXD3 (GenScript, clone ID OHu14665) or the empty vector using calcium phosphate. At 24 h, the cells were counted and seeded on 96-well plates previously covered with polylysine. After one day, Ag_5 was added at the indicated amounts for 1 h, washed and cells were allowed to grow for additional 24 h. Cell viability was measured by the MTT assay. PRXD3 overexpression was checked by western blot.

Correlation Between PRDX3 mRNA Expression and Ag_5 Sensitivity: An ED50 value was obtained for each cell line by fitting a two-parametric log-logistic model with lower limit at 0 and upper limit at 1 using the drm package[69] to cell viability values relative to the negative control, as a function of drug concentration. Gene expression data were obtained from https://depmap.org/portal/download, Version 20Q2[70] and available for 85 of our cell lines. Their correlation was assessed using Spearman's rank correlation implemented in the cor.test function of R.

Determination of ROS Using Fluorescent Dyes: H_2DCFDA staining. A549 (3×10^4 cells per well) and A2780 (3.5×10^4 cell per well) were seeded in 24-well plate and allowed to grow for 24 or 96 h for proliferating and nonproliferating cells. W3T3 RasV12 (5×10^4 cells per well) were seeded in 12-well plates. Then, cells were trypsinized, washed with PBS and incubated with CM-H_2DCFDA for 30 min at 37 °C. Stained cells were analyzed using the Guava EasyCyte flow cytometer and processed with the FlowJo program.

Immunoblotting: Unless specified, protein extracts from cultured cells were extracted using RIPA buffer with protease inhibitor cocktail (Sigma). After the electrophoresis proteins were transferred to PVDF membranes and blotted against the indicated antibodies.

PDRX3 and GR Assay: For the isolated mitochondria assays, mitochondria (0.5 mg mL^{-1}) were incubated in KCl buffer supplemented with glutamate/malate 5×10^{-3} M and different doses of Ag_5 or $AgNO_3$ at 37 °C for 5 min. After that, methyl methanethiosulfonate (MMTS) was added up to 80×10^{-3} M. Then samples were centrifuged at $7500 \times g$ for 5 min. The supernatants were removed, and the pellets suspended in loading buffer with MMTS (80×10^{-3} M) and heated at 95 °C for 5 min. Protein was determined by western blotting with anti-PRDX3. Membrane was visualized with an Odyssey CLx.

For the cell assays, A549 cells (2×10^6 cells) were seeded on 100 mm cell culture dishes and 24 h later treated with Ag_5 (37.7×10^{-6} M) in a 1:50 dilution for 15 min. Then, the treatment was removed and medium with MMTS (80×10^{-3} M) was added to the dish and incubated for 10 min at room temperature. After that, cells were washed with cold PBS and lysed with RIPA buffer with protease inhibitor cocktail containing MMTS (80×10^{-3} M) in nonreducing conditions. To quantify the amount of protein, an untreated control was performed without MMTS. After that, western blotting was performed by using anti-PRDX and anti-GR.

Immunofluorescence: A549 (3×10^4 cells per well), A2780 (8×10^4 cells per well), and HEK293T (8×10^4 cells per well) cells were grown on 24 mm coverslips and 24 h later treated with: 1) Ag_5 (IC_{50}) for 10 or 30 min, 2) DTT (0.5×10^{-3} M) for 10 min, 3) Ag_5 (IC_{50}) and DTT (0.5×10^{-3} M) for 10 min, and 4) NEM (100×10^{-6} M) for 30 min. After treatment, cells were washed with PBS, fixed in formalin solution (10%) for 30 min, washed with PBS and permeabilized with 0.5% Triton X-100 in PBS for 5–10 min. Then cells were washed again and blocked in PBS containing 1% BSA for 1 h. After that, samples were incubated with the primary antibodies anti-Keap1 (overnight at 4 °C) or anti-MTF1 (2 h at room temperature). Following washing with PBS, the samples were incubated for 45 min with the corresponding secondary antibody, AlexaFluor-488 donkey anti-goat for Keap, AlexaFluor-594 goat anti-rabbit for MTF1 and Hoechst (to counterstain the nucleus). Then, for double staining NRF2/Keap1, the cells were washed and incubated with the primary antibody against NRF2 for 2 h at room temperature, washed with PBS and incubated with the AlexaFluor-594 goat anti-rabbit and Hoechst (to counterstain the nucleus) for 45 min. Coverslips with stained cells were mounted on glass slides with Fluoroshield Mounting Medium. Images were obtained using the Olympus IX51 microscope equipped with an Olympus DP72 camera and CellSens Imaging Software and processed with ImageJ or the Leica TCS SP8 confocal microscope and analyzed using LasX software.

Caspase 3–7 Assay: A549 cells (3×10^4) were seeded in 24-well plate and 24 h later cells were treated with Ag_5 (IC_{50}), in the presence of the CellEvent Caspase 3/7 reagent (8×10^{-6} M). Time-lapse images were acquired every minute during 1 h using an inverted Leica DMI600B Wide-Field microscope equipped with an Okolab incubator controlled by an Okolab temperature controller and a DFC360FX Camera. Images were processed with the LAS AF software.

Annexin-V Assay: A549 (6×10^4) cells were seeded in 12-well plate and 24 h later treated with Ag_5 (IC_{50}) for 30 min. Then, cells were washed twice with PBS and stained with Annexin V-FITC and 7-AAD following manufacturer´s instructions. Images were obtained using Olympus IX51 microscope equipped with an Olympus DP72 camera and CellSens Imaging Software and processed with ImageJ.

Cell Irradiation: Cells were irradiated with 6 MV X-Ray beams generated by a Varian Medical Systems (Palo Alto, California) CLINAC 2100 C/D High energy linear accelerator at Radiation Physics Laboratory of University of Santiago de Compostela (http://www.usc.es/rpl). Absorbed dose to cells was determined by ionometric dosimetry corrected by Monte Carlo simulations. Irradiations were carried out by placing cells in 24-well plates surrounded by water equivalent plastic for electronic build up. A549 (3×10^4 cells per well) were seed in 24-well plates and allowed to grow for 96 h until they reach confluence (nonproliferative state). Then, cells were treated with Ag_5 (1.5×10^{-6}, 2×10^{-6}, 2.2×10^{-6} M) for 10 min and irradiated. Target absorbed doses (between 2 and 6 Gy) were delivered by single fractions at a rate of 2 Gy min^{-1}. After irradiation, cells were incubated with Ag_5 until complete 1 h of treatment and then trypsinized and reseeded for colony formation. 8 days later, cultures were fixed with crystal violet and colonies (>50 cells) were counted. Survival fractions (SF) were fitted to the linear quadratic model using GraphPad Prism 5 software (GraphPad Prism Software Inc., La Jolla, CA, USA).

DNA Damage Assay: DNA damage following irradiation was determined by the extent of phosphorylation of the histone protein γH2AX. A549 cells (3×10^4 cells) were seeded in 24-well plate. After

96 h, cells were treated with Ag_5 (1.5×10^{-6}, 2×10^{-6}, 2.2×10^{-6} M) for 10 min and irradiated. Then, cells were collected and DNA damage was measured using the p-H2AX (ser 139) FITC-conjugate antibody as described previously.[14] Stained cells were analyzed on Guava EasyCyte flow cytometer using InCyte program.

RNA Extraction, Reverse Transcription, and Quantitative Real-Time PCR (qRT-PCR): MM.1S cells (4×10^6) were seeded in 60 mm culture dishes and treated with Ag_5 (IC_{50}) for 30 min. Then, treatment was removed and 4 h later cells were collected, and their RNA isolated using the kit NucleoSpin ARN (Macherey-Nagel) following the manufacturer instructions. Reverse transcription was performed using the M-MLV reverse transcriptase, according to the manufacturer's instructions and analyzed by qRT-PCR using the TaqMan chemistry. Relative changes in gene expression were determined using the $2^{-\Delta\Delta Ct}$ method.[71]

Multicellular Tumoroids: A549 and HCT116 multicellular tumoroids were generated by the hanging-drop method as described previously.[72] 500 cells/20 µL were dispensed into each well of a MicroWell MiniTray (Nunc). At day 5 upon the inversion of the tray, spheroids were transferred to a 96-well plate coated with agarose (1%) and treated with Ag_5 four times on alternate days. To monitor spheroids growth images of each spheroid were taken every day using an Olympus IX51 microscope. Spheroid's area was measured using ImageJ. At the end of the experiment, A549 spheroids were stained with Image-iT Green Hypoxia Reagent 5×10^{-6} M and Hoechst (1 µg μL^{-1}) for 1 h. Images of control and treated spheroids were taken on a Leica AOBS-SP5 confocal microscopy and analyzed using ImageJ software. HCT116 spheroids were stained with CellEvent Caspase 3/7 reagent (8×10^{-6} M), Propidium iodide (1 µg μL^{-1}) and Hoechst (1 µg μL^{-1}) for 30 min. Then the spheroids were mixed with low-melt agarose solution (1%), the mixture was sucked into 1 mL syringes (diameter 1 mm) and allowed to gel at room temperature. After that the agarose blocks containing spheroids were imaged using Light Sheet Fluorescence Microscopy (LMSF Carl Zeiss Microscopy GmbH) and the images were processed using the Imaris Cell Imaging Software.

Statistical Analysis: All statistical analyses were performed with GraphPad Prism Version 5.0 software (GraphPad Software, Inc., La Jolla, USA). The differences were considered significant for $p < 0.05$. A two-way ANOVA with Bonferroni's correction was used for multiple group comparisons. Comparisons between two groups were analyzed using the 2-tailed Student's test. Mann–Whitney test was used for mice experiments.

Supporting Information

Supporting Information is available from the Wiley Online Library or from the author.

Acknowledgements

V.P. and D.B. contributed equally to this work. This research was partially supported by 1) "la Caixa" Foundation, Ref. LCF/PR/PR12/11070003 to F.D. and M.A.L.Q.; 2) Ministerio de Ciencia, Innovación y Universidades (MAT2017-89678-R, AEI/FEDER, UE) to F.D. and A.V.; 3) the Consellería de Educación (Xunta de Galicia), Grants No. Grupos Ref. Comp. ED431C 2017/22, ED431C 2019/13 and AEMAT-ED431E2018/08 to M.A.L.Q.; and ED431C 2019/13 to A.V. This project has received funding from the European Union's Horizon 2020 Research and Innovation Programme (Bac-To-Fuel) under Grant Agreement No. 825999 (M.A.L.Q.). J.C.H. acknowledge financial support from European Union's Horizon 2020 research and innovation programme under grant agreement no. 823717-ESTEEM3, and the MICIIN (projects PID2019-107578GA-100 and PID-110018GA-100). J.M.D, L.J.G., and F.G.R. thank to the ANPCyT (PICT 2015-2285 and 2017-3944), UNLP (Project 11/X790) and the partial support by the Laboratório Nacional de Luz Síncrotron (LNLS, Brazil) under proposal SXS-20180280. G.B. acknowledges the CINECA Award N. IsC51, year 2017, under the ISCRA initiative, for the availability of high-performance computing resources and support. D.B. expresses gratitude for a postdoctoral grant from Xunta de Galicia, Spain (POS-A/2013/018). B.D. expresses gratitude for a predoctoral grant from MICINN, Spain (BES-2016-076765). F.D. and A.V. also acknowledged Xunta de Galicia (Centro singular de investigación de Galicia accreditation 2019-2022 ref ED431G 2019/02) and the European Union (European Regional Development Fund – ERDF). Work in M.P.M.'s lab was supported by the Medical Research Council UK (MC_U105663142). T.G.C. gratefully acknowledges the technical assistance of María José Otero-Fraga (FIDIS).

Conflict of Interest

M.A.L.Q. and F.D. are scientific advisors and shareholders of Arjuna Therapeutics. M.A.L.Q., F.D, and D.B. have patents on cluster synthesis and therapeutical applications.

Data Availability Statement

The data that support the findings of this study are available on request from the corresponding author. The data are not publicly available due to privacy or ethical restrictions.

Keywords

cancer therapy, catalysis, low atomicity clusters, silver clusters, sulfur oxidation

Received: December 20, 2021
Revised: February 16, 2022
Published online:

[1] L. B. Sullivan, D. Y. Gui, A. M. Hosios, L. N. Bush, E. Freinkman, M. G. Vander Heiden, *Cell* **2015**, *162*, 552.
[2] K. Birsoy, T. Wang, W. W. Chen, E. Freinkman, M. Abu-Remaileh, D. M. Sabatini, *Cell* **2015**, *162*, 540.
[3] M. Bajzikova, J. Kovarova, A. R. Coelho, S. Boukalova, S. Oh, K. Rohlenova, D. Svec, S. Hubackova, B. Endaya, K. Judasova, A. Bezawork-Geleta, K. Kluckova, L. Chatre, R. Zobalova, A. Novakova, K. Vanova, Z. Ezrova, G. J. Maghzal, S. Magalhaes Novais, M. Olsinova, L. Krobova, Y. J. An, E. Davidova, Z. Nahacka, M. Sobol, T. Cunha-Oliveira, C. Sandoval-Acuña, H. Strnad, T. Zhang, T. Huynh, et al., *Cell Metab.* **2019**, *29*, 399.e10.
[4] I. Martínez-Reyes, L. R. Cardona, H. Kong, K. Vasan, G. S. McElroy, M. Werner, H. Kihshen, C. R. Reczek, S. E. Weinberg, P. Gao, E. M. Steinert, R. Piseaux, G. R. S. Budinger, N. S. Chandel, *Nature* **2020**, *585*, 288.
[5] M. P. Murphy, *Biochem. J.* **2009**, *417*, 1.
[6] H. Sies, D. P. Jones, *Nat. Rev. Mol. Cell Biol.* **2020**, *21*, 363.
[7] C. C. Winterbourn, *Antioxidants Redox Signal.* **2018**, *29*, 541.
[8] L. M. Booty, J. M. Gawel, F. Cvetko, S. T. Caldwell, A. R. Hall, J. F. Mulvey, A. M. James, E. C. Hinchy, T. A. Prime, S. Arndt, C. Beninca, T. P. Bright, M. R. Clatworthy, J. R. Ferdinand, H. A. Prag, A. Logan, J. Prudent, T. Krieg, R. C. Hartley, M. P. Murphy, *Cell Chem. Biol.* **2019**, *26*, 449.e8.
[9] I. S. Harris, A. E. Treloar, S. Inoue, M. Sasaki, C. Gorrini, K. C. Lee, K. Y. Yung, D. Brenner, C. B. Knobbe-Thomsen, M. A. Cox, A. Elia, T. Berger, D. W. Cescon, A. Adeoye, A. Brüstle, S. D. Molyneux, J. M. Mason, W. Y. Li, K. Yamamoto, A. Wakeham, H. K. Berman, R. Khokha, S. J. Done, T. J. Kavanagh, C. W. Lam, T. W. Mak, *Cancer Cell* **2015**, *27*, 211.

[10] A. Corma, P. Concepción, M. Boronat, M. J. Sabater, J. Navas, M. J. Yacaman, E. Larios, A. Posadas, M. A. López-Quintela, D. Buceta, E. Mendoza, G. Guilera, A. Mayoral, *Nat. Chem.* **2013**, *5*, 775.
[11] P. Jena, Q. Sun, *Chem. Rev.* **2018**, *118*, 5755.
[12] I. Chakraborty, T. Pradeep, *Chem. Rev.* **2017**, *117*, 8208.
[13] R. Jin, C. Zeng, M. Zhou, Y. Chen, *Chem. Rev.* **2016**, *116*, 10346.
[14] V. Porto, E. Borrajo, D. Buceta, C. Carneiro, S. Huseyinova, B. Domínguez, K. J. E. Borgman, M. Lakadamyali, M. F. Garcia-Parajo, J. Neissa, T. García-Caballero, G. Barone, M. C. Blanco, N. Busto, B. García, J. M. Leal, J. Blanco, J. Rivas, M. A. López-Quintela, F. Domínguez, *Adv. Mater.* **2018**, *30*, 1801317.
[15] D. Buceta, N. Busto, G. Barone, J. M. J. M. Leal, F. Domínguez, L. J. L. J. Giovanetti, F. G. F. G. Requejo, B. García, M. A. López-Quintela, M. A. López-Quintela, *Angew. Chem., Int. Ed.* **2015**, *54*, 7612.
[16] J. D. Sies, *Nat. Rev. Mol. Cell Biol.* **2020**, *21*, 363.
[17] M. P. Murphy, R. C. Hartley, *Nat. Rev. Drug Discovery* **2018**, *17*, 865.
[18] B. D'Autréaux, M. B. Toledano, *Nat. Rev. Mol. Cell Biol.* **2007**, *8*, 813.
[19] C. C. Winterbourn, M. B. Hampton, *F. Radic. Biol. Med.* **2008**, *45*, 549.
[20] M. Deponte, *Biochim. Biophys. Acta – Gen. Subj.* **2013**, *1830*, 3217.
[21] M. Gutscher, A. L. Pauleau, L. Marty, T. Brach, G. H. Wabnitz, Y. Samstag, A. J. Meyer, T. P. Dick, *Nat. Methods* **2008**, *5*, 553.
[22] N. Foloppe, L. Nilsson, *Structure* **2004**, *12*, 289.
[23] S. G. Rhee, *Mol. Cells* **2016**, *39*, 1.
[24] L. E. S. Netto, F. Antunes, *Mol. Cells* **2016**, *39*, 65.
[25] T. Parasassi, R. Brunelli, G. Costa, M. De Spirito, E. K. Krasnowska, T. Lundeberg, E. Pittaluga, F. Ursini, *Sci. World J.* **2010**, *10*, 1192.
[26] O. W. Griffith, *J. Biol. Chem.* **1982**, *257*, 13704.
[27] S. J. Dixon, D. Patel, M. Welsch, R. Skouta, E. Lee, M. Hayano, A. G. Thomas, C. Gleason, N. Tatonetti, B. S. Slusher, B. R. Stockwell, *Elife* **2014**, *3*, e02523.
[28] H. Ogiwara, K. Takahashi, M. Sasaki, T. Kuroda, H. Yoshida, R. Watanabe, A. Maruyama, H. Makinoshima, F. Chiwaki, H. Sasaki, T. Kato, A. Okamoto, T. Kohno, *Cancer Cell* **2019**, *35*, 177.e8.
[29] M. B. Hampton, K. M. O'Connor, *Mol. Cells* **2016**, *39*, 72.
[30] A. G. Cox, K. K. Brown, E. S. J. Arner, M. B. Hampton, *Biochem. Pharmacol.* **2008**, *76*, 1097.
[31] I. S. Song, H. K. Kim, S. H. Jeong, S. R. Lee, N. Kim, B. D. Rhee, K. S. Ko, J. Han, *Int. J. Mol. Sci.* **2011**, *12*, 7163.
[32] C. Gorrini, I. S. Harris, T. W. Mak, *Nat. Rev. Drug Discovery* **2013**, *12*, 931.
[33] C. R. Reczek, N. S. Chandel, *Annu. Rev. Cancer Biol.* **2017**, *1*, 79.
[34] X. Ren, L. Zou, J. Lu, A. Holmgren, *F.Radic. Biol. Med.* **2018**, *127*, 238.
[35] A. Simons, D. Mattson, K. Dornfeld, D. Spitz, *J. Cancer Res. Ther.* **2009**, *5*, 2.
[36] K. Psenakova, R. Hexnerova, P. Srb, V. Obsilova, V. Veverka, T. Obsil, *FEBS J.* **2020**, *287*, 1626.
[37] M. Rojo de la Vega, E. Chapman, D. D. Zhang, *Cancer Cell* **2018**, *34*, 21.
[38] G. K. Andrews, *Biochem. Pharmacol.* **2000**, *59*, 95.
[39] R. Hayakawa, T. Hayakawa, K. Takeda, H. Ichijo, *Proc. Japan Acad., Ser. B: Phys. Biol. Sci.* **2012**, *88*, 434.
[40] D. N. Dhanasekaran, E. P. Reddy, *Oncogene* **2008**, *27*, 6245.
[41] K. Irani, Y. Xia, J. L. Zweier, S. J. Sollott, C. J. Der, E. R. Fearon, M. Sundaresan, T. Finkel, P. J. Goldschmidt-Clermont, *Science* **1997**, *275*, 1649.
[42] A. Luengo, D. Y. Gui, M. G. Vander Heiden, *Cell Chem. Biol.* **2017**, *24*, 1161.
[43] F. Weinberg, R. Hamanaka, W. W. Wheaton, S. Weinberg, J. Joseph, M. Lopez, B. Kalyanaraman, G. M. Mutlu, G. R. S. Budinger, N. S. Chandel, *Proc. Natl. Acad. Sci. USA* **2010**, *107*, 8788.
[44] C. T. Hensley, B. Faubert, Q. Yuan, N. Lev-Cohain, E. Jin, J. Kim, L. Jiang, B. Ko, R. Skelton, L. Loudat, M. Wodzak, C. Klimko, E. McMillan, Y. Butt, M. Ni, D. Oliver, J. Torrealba, C. R. Malloy, K. Kernstine, R. E. Lenkinski, R. J. DeBerardinis, *Cell* **2016**, *164*, 681.
[45] J. Kim, R. J. DeBerardinis, *Cell Metab.* **2019**, *30*, 434.
[46] J. Friedrich, C. Seidel, R. Ebner, L. A. Kunz-Schughart, *Nat. Protoc.* **2009**, *4*, 309.
[47] M. Zanoni, F. Piccinini, C. Arienti, A. Zamagni, S. Santi, R. Polico, A. Bevilacqua, A. Tesei, *Sci. Rep.* **2016**, *6*, 19103.
[48] A. I. Minchinton, I. F. Tannock, *Nat. Rev. Cancer* **2006**, *6*, 583.
[49] E. Borrajo, R. Abellan-Pose, A. Soto, M. Garcia-Fuentes, N. Csaba, M. J. Alonso, A. Vidal, *J. Controlled Release* **2016**, *238*, 263.
[50] U. E. Martinez-Outschoorn, M. Peiris-Pagés, R. G. Pestell, F. Sotgia, M. P. Lisanti, *Nat. Rev. Clin. Oncol.* **2017**, *14*, 11.
[51] T. Van Den Beucken, E. Koch, K. Chu, R. Rupaimoole, P. Prickaerts, M. Adriaens, J. W. Voncken, A. L. Harris, F. M. Buffa, S. Haider, M. H. W. Starmans, C. Q. Yao, M. Ivan, C. Ivan, C. V. Pecot, P. C. Boutros, A. K. Sood, M. Koritzinsky, B. G. Wouters, *Nat. Commun.* **2014**, *5*, 5203.
[52] L. M. Minassian, T. Cotechini, E. Huitema, C. H. Graham, in *Advances in Experimental Meddicine and Biology*, Springer, New York **2019**, pp. 123–139.
[53] M. Abbate, F. C. Vicentin, V. Compagnon-Cailhol, M. C. Rocha, H. Tolentino, *J. Synchrotron Radiat.* **1999**, *6*, 964.
[54] A. Vairavamurthy, *Spectrochim. Acta, Part A: Mol. Biomol. Spectrosc.* **1998**, *54*, 2009.
[55] A. D. Becke, *Cit. J. Chem. Phys* **1993**, *98*, 5648.
[56] C. Lee, W. Yang, R. G. Parr, *Phys. Rev. B* **1988**, *37*, 785.
[57] P. C. Hariharan, J. A. Pople, *Theor. Chim. Acta* **1973**, *28*, 213.
[58] M. M. Francl, W. J. Pietro, W. J. Hehre, J. S. Binkley, M. S. Gordon, D. J. DeFrees, J. A. Pople, *J. Chem. Phys.* **1982**, *77*, 3654.
[59] P. J. Hay, W. R. Wadt, *J. Chem. Phys.* **1985**, *82*, 270.
[60] L. W. Chung, W. M. C. Sameera, R. Ramozzi, A. J. Page, M. Hatanaka, G. P. Petrova, T. V. Harris, X. Li, Z. Ke, F. Liu, H. B. Li, L. Ding, K. Morokuma, *Chem. Rev.* **2015**, *115*, 5678.
[61] A. K. Rappé, C. J. Casewit, K. S. Colwell, W. A. Goddard, W. M. Skiff, *J. Am. Chem. Soc.* **1992**, *114*, 10024.
[62] M. Cossi, N. Rega, G. Scalmani, V. Barone, *J. Comput. Chem.* **2003**, *24*, 669.
[63] C. Peng, H. B. Schlegel, *Isr. J. Chem.* **1993**, *33*, 449.
[64] J. Frisch, G. W. Trucks, H. B. Schlegel, G. E. Scuseria, M. A. Robb, J. R. Cheeseman, J. A. M. Jr., T. Vreven, K. N. Kudin, J. C. Burant, J. M. Millam, S. S. Iyengar, J. Tomasi, V. Barone, B. Mennucci, M. Cossi, G. Scalmani, N. Rega, G. A. Petersson, H. Nakatsuji, M. Hada, M. Ehara, K. Toyota, R. Fukuda, J. Hasegawa, M. Ishida, T. Nakajima, Y. Honda, O. Kitao, H. Nakai, et al., *Gaussian 09, Revision A.01*, Gaussian Inc., Wallingford, CT **2009**.
[65] A. L. Smith, *Methods Enzymol.* **1967**, *10*, 81.
[66] J. E. Walker, J. M. Skehel, S. K. Buchanan, *Methods Enzymol.* **1995**, *260*, 14.
[67] B. Cunniff, G. W. Snider, N. Fredette, R. J. Hondal, N. H. Heintz, *Anal. Biochem.* **2013**, *443*, 34.
[68] R. Zhao, H. Masayasu, A. Holmgren, *Proc. Natl. Acad. Sci. USA* **2002**, *99*, 8579.
[69] C. Ritz, F. Baty, J. C. Streibig, D. Gerhard, *PLoS One* **2015**, *10*, e0146021.
[70] M. Ghandi, F. W. Huang, J. Jané-Valbuena, G. V. Kryukov, C. C. Lo, E. R. McDonald, J. Barretina, E. T. Gelfand, C. M. Bielski, H. Li, K. Hu, A. Y. Andreev-Drakhlin, J. Kim, J. M. Hess, B. J. Haas, F. Aguet, B. A. Weir, M. V. Rothberg, B. R. Paolella, M. S. Lawrence, R. Akbani, Y. Lu, H. L. Tiv, P. C. Gokhale, A. de Weck, A. A. Mansour, C. Oh, J. Shih, K. Hadi, Y. Rosen, et al., *Nature* **2019**, *569*, 503.
[71] M. W. Pfaffl, *Nucleic Acids Res.* **2002**, *30*, 36e.
[72] N. E. Timmins, L. K. Nielsen, *Methods Mol. Med.* **2007**, *140*, https://doi.org/10.1007/978-1-59745-443-8_8.